



HAL
open science

Mechanical and Nanomechanical Properties

Christophe Tromas, Marc Verdier, Marc Fivel, Pierre-Henri Aubert, Sid Labdi, Zhi-Qiang Feng, Maria Zei, Pierre Joli

► **To cite this version:**

Christophe Tromas, Marc Verdier, Marc Fivel, Pierre-Henri Aubert, Sid Labdi, et al.. Mechanical and Nanomechanical Properties. Catherine Bréchnignac; Philippe Houdy; Marcel Lahmani. Nanomaterials and Nanochemistry, Springer Verlag, pp.229-265, 2007, 978-3-540-72992-1. 10.1007/978-3-540-72993-8_8. hal-00342997

HAL Id: hal-00342997

<https://hal.science/hal-00342997>

Submitted on 30 Oct 2023

HAL is a multi-disciplinary open access archive for the deposit and dissemination of scientific research documents, whether they are published or not. The documents may come from teaching and research institutions in France or abroad, or from public or private research centers.

L'archive ouverte pluridisciplinaire **HAL**, est destinée au dépôt et à la diffusion de documents scientifiques de niveau recherche, publiés ou non, émanant des établissements d'enseignement et de recherche français ou étrangers, des laboratoires publics ou privés.

Mechanical and Nanomechanical Properties

C. Tromas, M. Verdier, M. Fivel, P. Aubert, S. Labdi, Z.-Q. Feng, M. Zei, and P. Joli

8.1 Macroscopic Mechanical Properties

8.1.1 Introduction

The growing interest in nanomaterials over the past decade or so can be put down to their unique structure, characterised by grains with nanometric dimensions and by a rather high density of crystal defects, which will undoubtedly lead to quite exceptional properties. In particular, extrapolating the constitutive laws of large-grained materials down to the nanoscale leads one to expect interesting mechanical behaviour for nanomaterials. Materials can be produced with high levels of hardness, ductility, and sometimes superplasticity (see Chap. 9) at relatively low temperatures. These characteristics lead to remarkable mechanical performance and machining possibilities, by virtue of which such nanomaterials have immediate scope for technological innovation.

Section 8.1 describes the main mechanical properties associated with nanostructured materials and also the mechanisms so far put forward to relate grain size to observed properties. The discussion here will be restricted to the measurement of structural properties such as elasticity, hardness, and ductility in ‘cold’ conditions, leaving the description of superplasticity in nanomaterials and properties of moulding in higher temperature regimes to Chap. 9. We shall discuss nanostructured bulk materials, i.e., three-dimensional bodies in which the crystallites have nanometric dimensions, and thin films, which are macroscopic in two dimensions but have submicron thickness and can be made up of grains with sizes much smaller than their thickness, or of successive layers of nanometric thickness (multilayer structures).

8.1.2 Elastic Properties

The elastic limit of a material (the stress beyond which a remanent plastic strain is observed) is intimately related to its elastic constants (see below).

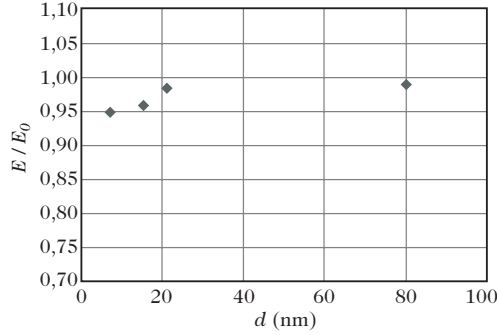


Fig. 8.1. Grain size dependence of the Young's modulus relative to that of large-grained polycrystals for Fe nanocrystals. From [1]

Indeed, a plastic strain only occurs in order to reduce the energy associated with the elastic strain of the material. The elastic constants reflect the nature and density of atomic bonds. In nanomaterials, the high density of structural defects and grain boundaries have an effect on the elastic constants. The first measurements of Young's modulus revealed a significant difference between nanostructured materials and the corresponding large-grained materials. In some cases the modulus was much higher, as for superlattices, and in others much lower, as for materials produced by sintering. However, it was subsequently demonstrated that these early results were due to experimental artifacts and often to the presence of defects, such as fractures and high porosity, introduced during fabrication and not properly taken into account when interpreting the observations. More recent results obtained on dense materials have finally shown that the Young's modulus gradually falls off only for grain sizes below 10 nm, i.e., when the fraction of atoms associated with grain boundary and triple junctions becomes very high (see Fig. 8.1).

However, the change in the modulus measured in this way never exceeds 10–20% of the value for the material with conventional grain size.

Mechanical Behaviour Under Tension

The elastic–plastic behaviour of a material is most commonly investigated by carrying out a uniaxial tensile test on a test bar. The tensile stress σ is defined as the ratio of the tensional force and the cross-sectional area of the test bar, i.e., $\sigma = F/S$. σ is expressed in megapascal (1 MPa = 1 N/mm²). The strain or deformation of the useful zone of the test bar is defined as $\varepsilon = \ln(l/l_0)$, where l and l_0 are the instantaneous length and the initial length of the bar, respectively. The curve is divided into two parts: an 'elastic' part in which any strain remains completely reversible, and a plastic part in which the test bar retains a permanent residual lengthening even when the load is removed.

Several quantities can be directly measured in a tensile test:

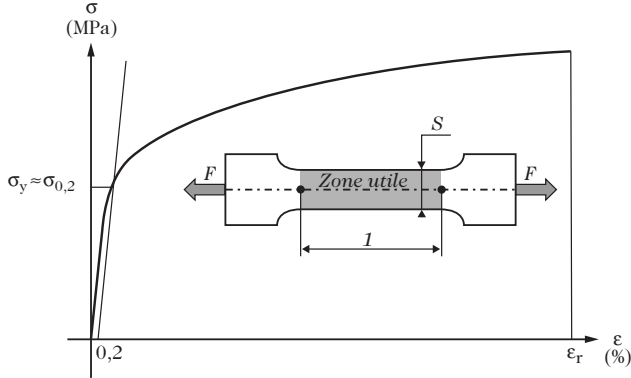


Fig. 8.2. Mechanical behaviour under tension

- The elastic limit σ_y , also called the yield point, beyond which plastic strain occurs. In practice, this transition point is difficult to determine and one measures instead the conventional elastic limit at $\sigma_{0.2}$ for which the plastic strain rate is 0.2%.
- Young's modulus E , the slope of the elastic strain region approximated by a straight line.
- The constriction coefficient Z , defined as the ratio $Z = (S_0 - S_u)/S_0$, where S_0 is the initial cross-sectional area of the useful zone of the test bar and S_u is its final cross-sectional area after rupture. A brittle material will have a value of Z close to zero, while a ductile material, with high strain capacity, will have a value of Z close to unity.
- The maximal strain ϵ_r sustainable by the test bar before rupture.

8.1.3 Hardness

The (Brinell) hardness H of a material is defined as the ratio between the load F applied to a hard ball and the residual indent A left in the material after withdrawing the load, i.e., $H = F/A$. The hardness is one of the most commonly measured mechanical characteristics of a nanomaterial. It is determined by a nanoindentation test, which is relatively easy to carry out (see below). This characteristic is often very useful for predicting the technological capabilities of the material, e.g., for thin protective films. This quantity is intrinsically related to the ability of the material to deform plastically. To a first approximation it can be related to the yield point σ_y of a material by the empirical relation $H = 3\sigma_y$.

Nanoindentation

The nanoindentation technique is a mechanical test derived from the standard hardness test. The idea is to sink a hard tip of known geometry into the material under

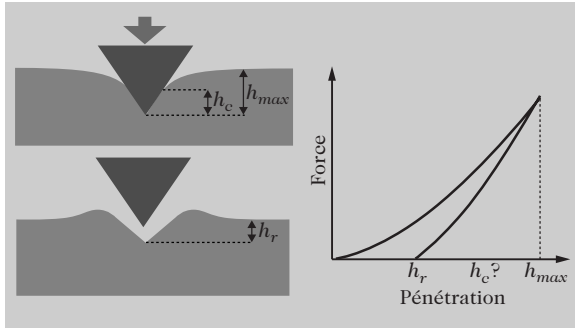


Fig. 8.3. Measuring hardness

investigation and monitor the depth of penetration as a function of the applied load. By carrying out a loading–unloading cycle, a characteristic force–penetration curve is obtained. By analysing the unloading curve and modelling the material as an elastic and isotropic continuous medium, one can deduce the relevant parameter here, which is the true contact area between the indenter and the material under maximal load. One can then deduce not only the hardness, but also the Young’s modulus of the material. The applied forces range from a few tenths to several hundred millinewtons, and the depths of penetration from a few nanometers to several microns.

In the case of large-grained materials, plastic strain corresponds to nucleation and/or motion of dislocation lines (see below) in the material. These lines then multiply via the Frank–Read mechanism. The stress needed to activate such a source depends on the distance separating the two points at which the dislocation is anchored. It is thus easy to see that reducing the grain size will also reduce the distances between such points and hence raise the elastic limit. The empirical Hall–Petch relation expresses this effect:

$$\sigma_y = \sigma_0 + \frac{k}{\sqrt{d}},$$

where σ_0 is a lattice friction stress, k a constant, and d the grain size. The proportionality between hardness and elastic limit can be used to define a relation of the same type between hardness and grain size. For large-grained materials, the Hall–Petch relation is explained by dislocations piling up along grain boundaries: plastic strain is triggered when the stress at the front of the dislocation pile-up is enough to activate a Frank–Read source in the neighbouring grain.

Extrapolating this law to grains of around ten nanometers, very high values of the hardness are predicted, the only limit being the theoretical limiting stress of a perfect crystal, generally taken as $G/10$, where G is the transverse shear modulus. However, although the hardness does indeed increase at small grain sizes, the observed effects are generally much smaller than would be predicted in this way, and at very small grain sizes, or for very small periods

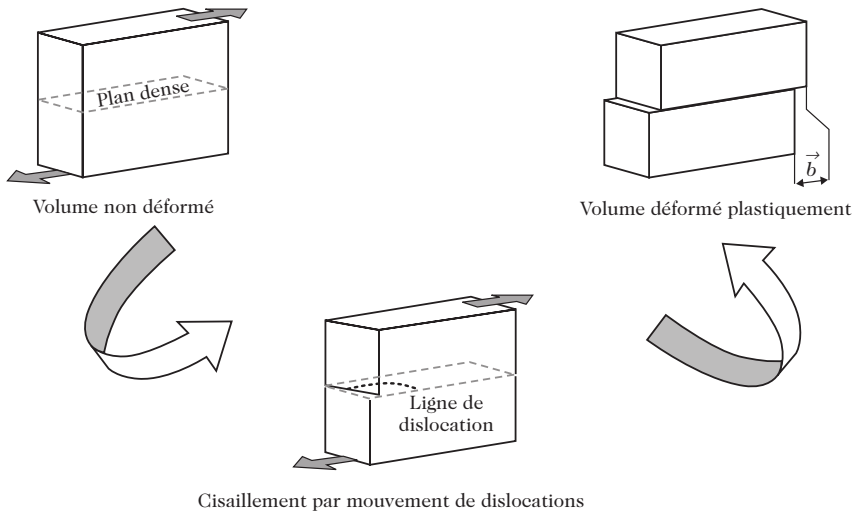


Fig. 8.4. Production of a dislocation

in the case of multilayer films, the opposite trend to the Hall–Petch relation is sometimes observed, i.e., a reduction in hardness with reduced grain size (or period). This ‘negative’ Hall–Petch effect has nevertheless been explained for nanocrystalline materials that have undergone thermal treatment, by invoking densification or phase transformation phenomena.

Whatever the case may be, for materials with grain sizes below 10 nm, the absence of mobile dislocations means that any models based on the behaviour of dislocations applying to large-grained materials are no longer relevant. The limits of the Hall–Petch effect in 3D nanomaterials have been demonstrated by several computer simulations. For grain sizes below a few nanometers, plasticity is no longer due to the motion of dislocations, but to a very large number of small amplitude slipping motions at grain boundaries.

Dislocations

When a material is subjected to stress, it begins by deforming in a reversible manner (elastic strain), then irreversibly, with permanent consequences (plastic strain). In the case of plastic strain in a crystalline material, the macroscopic change in shape as seen from the outside must occur without altering the periodic arrangement of the crystal lattice on the atomic scale. This is only possible via a series of shears with amplitude proportional to the size of the unit cell in the atomic lattice, in such a way that the crystal structure is reinstated after each shear. However, calculation shows that such shear transformations cannot occur simultaneously throughout the material, because this would require stresses more than a thousand times stronger than those observed. If we imagine a shear with amplitude of the order of the lattice parameter which has propagated over only a part of the crystal, the line defining the boundary of the sheared region is a linear crystal defect called a dislocation.

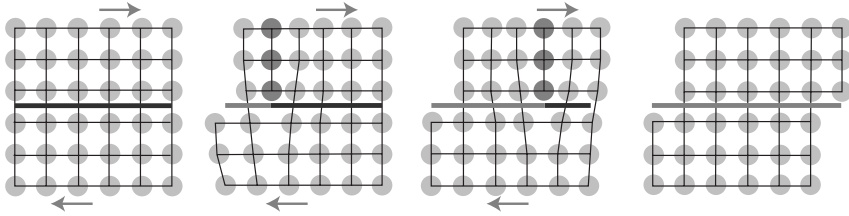


Fig. 8.5. Motion of an edge dislocation. The dislocation line runs perpendicular to the plane of the figure and marks the boundary between the region already sheared (*light grey*) and the unsheared region (*dark grey*)

Figure 8.5 then shows how the displacement of a dislocation will propagate the shear through the crystal, whilst leaving the crystallographic structure intact behind it. This is called an edge or screw dislocation depending on whether the direction \mathbf{b} of the propagated shear is perpendicular or parallel to the dislocation line.

The shear plane in which the dislocation moves is called the slip plane of the dislocation. It corresponds to a close-packed plane of the crystal lattice, i.e., one containing the greatest number of atoms. The amplitude and direction of the shear propagated by the dislocation are characterised by the so-called Burgers vector \mathbf{b} of the dislocation. Dislocations play a major role in the mechanical behaviour of conventional materials through their density, mobility and interactions.

The same kind of behaviour is found in 2D nanomaterials. Hence, in structures composed of layers of different materials, large increases in hardness can be observed, well above those predicted by the law of mixing. These systems have several points in common, such as an increase in hardness when the period of the bilayer is reduced, at least down to 4 nm. This phenomenon can be explained by a behavioural model similar to the Hall–Petch law. These increases in hardness reflect the resistance to motion of dislocations in each of the layers making up the multilayer structure. However, discrepancies are sometimes observed with respect to the Hall–Petch law for layer thicknesses below 20 nm, as illustrated in Fig. 8.6.

Such discrepancies from the Hall–Petch law have not yet been fully explained, but changes in the chemical nature of the interface may be relevant for quasi-monatomic layers. In any case, observations using atomic force microscopy clearly show a change in the plastic strain mode: slip bands visible for thicknesses above 20 nm are no longer observed at smaller thicknesses (see Fig. 8.7).

8.1.4 Ductility

Ductility is the ability of a material to change shape without fracture. This property is extremely important as regards technological applications of materials, whether it be for their performance in use or the ease with which they can be worked. The effect of grain size on ductility is well understood for

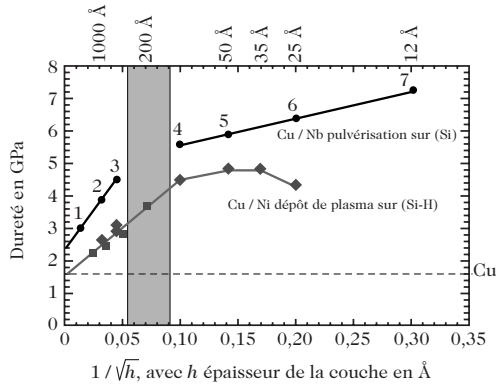


Fig. 8.6. Example of deviation from the Hall–Petch law in the case of alternating Cu/Ni multilayers obtained by plasma deposition and Cu/Nb multilayers deposited on an Ni substrate. Taken from [2]

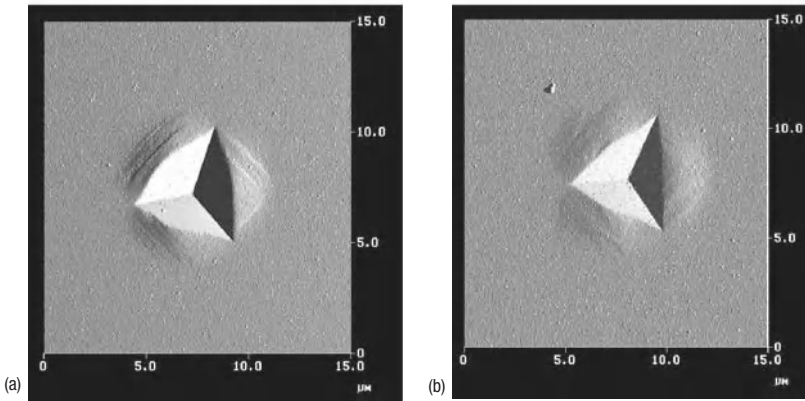


Fig. 8.7. AFM observations of the residual indent from a 150-nm indentation of a Cu/Ni multilayer. (a) Alternating layers of thickness 50 nm. (b) Layers of thickness 2.5 nm

materials with micrometric grains. For example, the brittle–ductile transition temperature in a steel can be lowered by 40°C by reducing the grain size by a factor of five. Extrapolation to the nanoscale promised extremely good ductility properties for nanomaterials, but it is a delicate matter to characterise a nanocrystalline material in this respect. This explains the many contradictory results encountered in the literature. Indeed, ductility reflects the possibility of plastic strain without fracture. However, fracture behaviour depends sensitively on the way the sample was prepared and on its final surface state, as well as the type of mechanical test used. In fact, fracture mechanisms depend sensitively on the tensile stresses in the material, and compression tests often prove inadequate for establishing the ductility.

For metals, which generally exhibit ductile behaviour when their microstructure comprises large grains, results obtained by tensile tests usually reveal brittle behaviour for grain sizes below 30 nm. This phenomenon can be explained by the major difficulty for dislocations to nucleate and slip inside such small grains.

Ceramic and intermetallic materials are conventionally brittle. The first studies of ceramics with nanocrystalline structure (CaF_2 and TiO_2) suggested that with nanometric grain sizes these materials might exhibit ductile behaviour at low temperatures. The hypothesis then made involved a creep mechanism by diffusion at the grain boundaries that would increase in importance at small grain sizes. Indeed, conventional models of creep predict a relation of the type

$$\dot{\epsilon} = \alpha \frac{\sigma^n}{d^p}$$

between the plastic strain rate $\dot{\epsilon}$, the creep stress σ , and the grain size d . For low temperature creep at grain boundaries, called Coble creep, it is generally found that $n = 1$ and $2 < p < 3$. According to this law, dividing the grain size by a factor of two would increase the creep rate by a factor of eight. However, the first results obtained on nanocrystalline CaF_2 and TiO_2 could not be reproduced. It seems likely that the ductile behaviour observed in these early studies were illusory and probably influenced by the high porosity of the samples used.

In the end, nanocrystalline materials did not live up to expectations with regard to improved ductility. However, interesting properties were reported for polyphase materials with nanometric structuring. An increase in the elastic limit is observed in these materials in conjunction with a good level of ductility. These effects were observed for alloys with partially crystallised microstructures, i.e., for nanocrystallites confined within an amorphous matrix, or more recently for micrometric copper grains embedded in a nanocrystalline copper matrix.

8.1.5 Numerical Modelling

It is often a difficult matter to determine mechanical properties of nanomaterials experimentally, and various techniques for producing the samples can lead to a problem of reproducibility in the results. This explains the contradictory results often encountered in the literature. Modern numerical tools provide new possibilities for exploring the mechanical properties of nanomaterials. However, in order to model the mechanical behaviour of nanomaterials correctly, experimentally observed size effects must be reproduced.

A great many numerical models are poorly suited to this task because devoid of any reference length. For example, the finite element methods so widely used in solid mechanics can only be used if the behavioural relations they employ involve a characteristic length able to account for size effects.

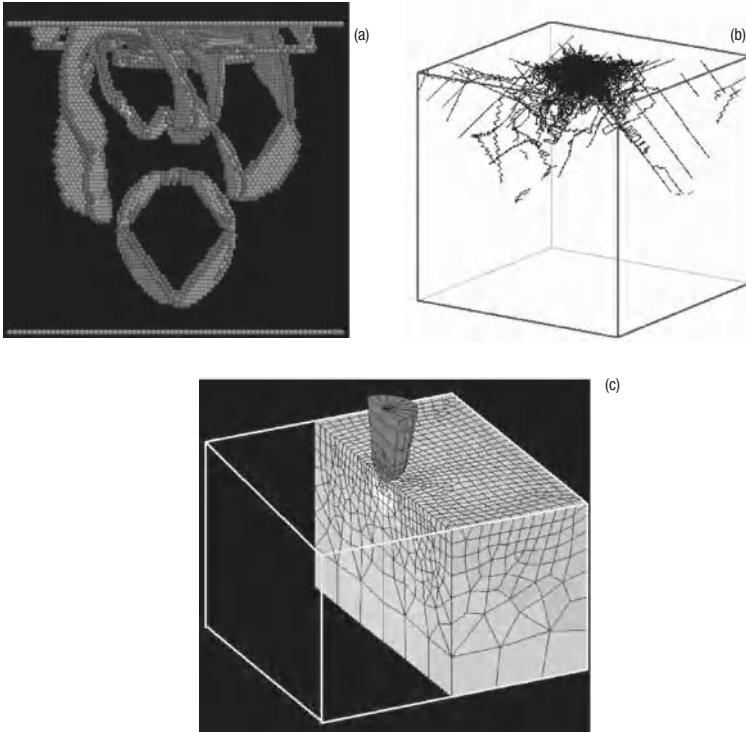


Fig. 8.8. Simulations of a nanoindentation test with a spherical tip. (a) Molecular dynamics. (b) Dislocation dynamics. (c) Finite elements. See also the colour plate

To achieve this, one can for example include strain gradients, and hence the second gradient of the displacement field, when expressing the constitutive laws. This naturally brings an internal length scale into the equations. These are called second gradient methods [3]. Another solution is to take into account the kinematics in a more detailed way, involving the strain modes of the material, e.g., motion of dislocations, lattice rotation, interaction with a magnetic moment, and so on, and also including an intrinsic length scale. This is exemplified by Cosserat media [4,5] and micropolar media [6], among others. In each simulation based on such a method, the internal length scale must be related to a characteristic length scale of the material, such as grain size, dimensions of microstructural elements, and so on.

On smaller length scales, of the order of the micron, recent models have been developed to simulate the collective behaviour of interacting populations of dislocations. These dislocation dynamics models are particularly well suited to handle plastic strain in nanomaterials when it is due to motion of dislocations. They lead naturally to scaling laws of Hall–Petch type.

At still smaller length scales, the methods of molecular dynamics can be used to calculate the positions of atoms in a crystal as a function of time. The appearance and multiplication of dislocations can then be simulated, together with any other mechanism leading to plastic strain. These methods can then be used to study alternative mechanisms of plastic strain that may come into play when grains have nanometric dimensions.

Figure 8.8 shows simulations of a nanoindentation test carried out using the three main families of simulation methods.

8.2 Nanomechanical Properties

8.2.1 Experimentation

Nanomechanical Characterisation by Nanoindentation: Hardness

Metallurgists have long been concerned with the problem of measuring hardness. Over time, many methods have been developed to measure this property. They can be classified into two main categories of tests [7]: dynamical hardness tests and static indentation tests. In a dynamical hardness test, a fixed load is dropped from a fixed height onto the surface. The hardness is expressed in terms of impact energy and size of indent. The quasi-static indentation method, which remains the most widely used, consists in pressing a very hard object with well defined geometry against the surface of the material under test. Depending on the load used, there are three techniques here: macroindentation (loads greater than 10 N), microindentation (loads in the range 0.1–10 N), and nanoindentation where loads are of the order of the mN.

The first two techniques cannot be used to measure the mechanical properties of very thin films and materials with surface treatments. Indeed, they simply crush and pierce the film and end up testing only the substrate. Today, technical progress in instruments capable of measuring nanometric displacements and others capable of applying and controlling loads of mN order have made nanoindentation into a genuine mechanical microprobe, widely used in the mechanical characterisation of thin films (see Fig. 8.9).

Basic Idea

In conventional indentation techniques, the residual indent is measured when the indenter has been withdrawn. The results of such tests are not easy to interpret. Indeed, there is no way of taking into account any relaxation in the material. Consequently, it is impossible to distinguish the elastic part, and this increases the uncertainty in the hardness measurement of ceramic materials characterised by a high degree of elasticity. In nanoindentation, continuous measurement of the load and displacement has replaced this simplistic measurement of the residual indent.

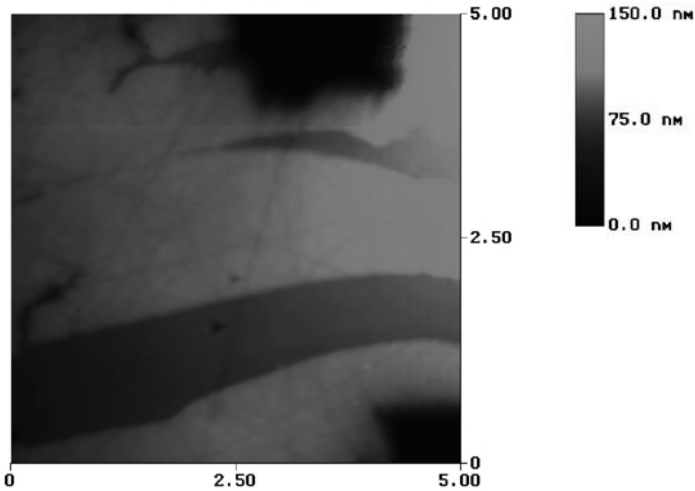


Fig. 8.9. Indentation in a deposit of alumina and titanium oxide obtained by plasma projection. See also the colour plate

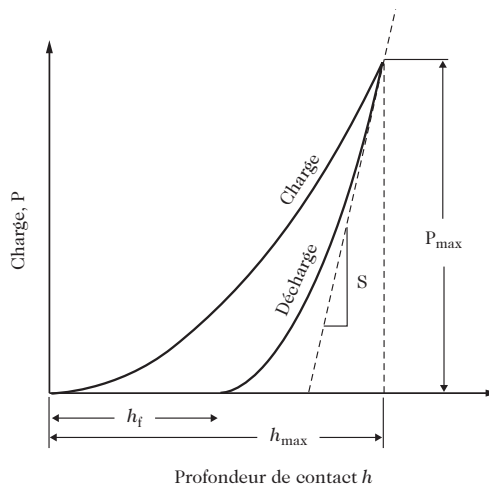


Fig. 8.10. Loading/unloading curve showing the relevant physical quantities

A typical loading/unloading curve is shown in Fig.8.10. The indenter, initially in contact with the surface, is driven into the material until a pre-determined maximal load or depth is reached, using a constant loading rate (loading cycle). The load is then reduced to zero at the same rate (unloading cycle).

The loading curve is characterised by an elastic-plastic regime and can be used to deduce the value of the hardness defined as the ratio of the maximal load to the area of contact between the indenter and the material at this load.

The unloading curve generally corresponds to a purely elastic regime. It can be used to deduce the Young's modulus.

Figure 8.10 shows the depth h_d defined by the intersection of the tangent to the unloading curve taken at the top of the curve with the horizontal axis. This tangent corresponds to the unloading curve that would have been obtained if the indenter had had plane geometry and the same area as the contact area at the maximum of the curve between a real indenter and the material.

Choice of Indenter

The indenter must have a high elastic modulus and no plastic strain at the contact pressures occurring during indentation, as well as a smooth surface and well defined geometry so that the indent itself will be well defined. Diamond is generally chosen for its satisfactory properties with regard to these requirements. In practice, it is very difficult to work indenters into a perfect geometry. The indenter thus exhibits irregularities that must be taken into account when calculating the contact pressure.

A Berkovich geometry is usually used for nanoindenters. This has pyramidal shape with triangular base. The Vickers indenter (pyramidal but with square base) is sometimes used when applied loads approach values used for microindentation. The advantage of the Berkovich indenter comes from the fact that it is more finely tapered than the Vickers indenter. Indeed, the radius of curvature is less than 50 nm for most commercially available Berkovich indenters at the present time. The two types of indenter do share one geometrical similarity, namely they have the same area function $A = f(h)$. For an ideal geometry, the area function is $A = 24.5h^2$.

Analysing the Loading/Unloading Curve

Figure 8.11 shows the response of an elastic–plastic material during indentation by a pyramidal indenter. In this figure, the depth of contact h_c is defined as the depth of penetration when the indenter is in contact with the sample. h is the depth measured during indentation. During indentation, h satisfies the relation

$$h = h_s + h_c , \quad (8.1)$$

where h_s is the displacement of the surface on the perimeter of the contact due to elastic depression. The maximal load and depth are denoted by P_{\max} and h_{\max} , respectively. After unloading and elastic recovery, the final depth of the residual indent is denoted by h_f .

The whole difficulty in interpreting the curve lies in determining the contact area between indenter and material for a given depth of penetration. Now the indenter geometry (area function) can be well established (using a calibration procedure to be described below) and it then suffices to determine

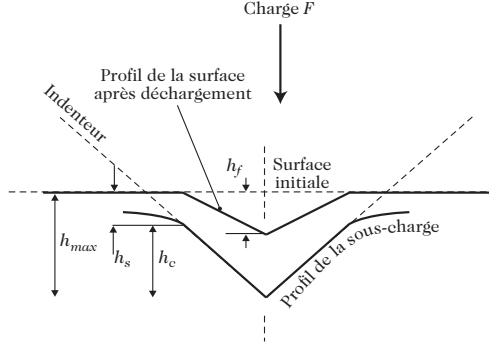


Fig. 8.11. Schematic representation of the indentation process illustrating the depression of the sample and reduction of penetration depth after unloading. From Oliver and Pharr [8]

the depth of contact in order to know the contact area. The problem thus reduces to determining the contact depth h_c .

The analysis described here and used by most commercial nanoindenters is the one developed by Oliver et Pharr [8] for elastoplastic materials.

Measuring Contact Rigidity S_{\max}

The unloading curve is analysed using the theory of elastic contact. This problem was treated by Hertz [16] and Boussinesq [17], but the theory most widely used today is the one developed by Sneddon, who established a relation between the load and the displacement:

$$P = Ch^m, \quad (8.2)$$

where C and m are constants ($m = 1$ for a cylindrical geometry, $m = 2$ for conical geometry, and $m = 1.5$ for spherical geometry).

Oliver and Pharr [8] noted that the unloading curve is better described by a power law similar to (8.13) in the term $h - h_f$, viz.,

$$P = \alpha(h - h_f)^m, \quad (8.3)$$

where the constants α , m and h_f are determined by a simple least-squares fitting method. The initial slope of the unloading curve can then be simply found by calculating the derivative of the curve analytically at maximal depth.

Calculating Young's Modulus

Tabor [9] was the first to use continuous monitoring of the load as a function of the displacement as a way of measuring hardness. One of the most important results was that the effect of the non-rigidity of the indenter can be taken into account by defining a reduced Young's modulus E_r by

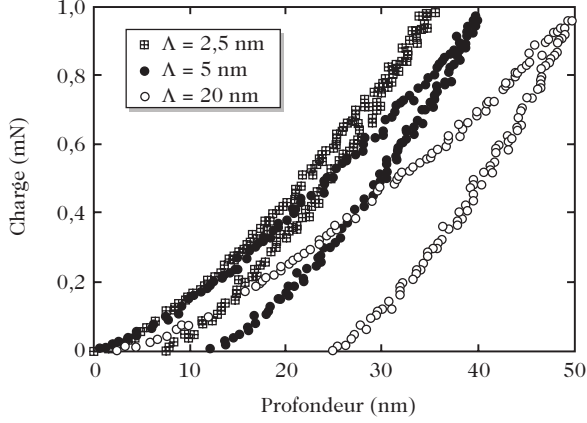


Fig. 8.12. Loading/unloading curve for Ti/TiN multilayers with variable periods at constant load 1 mN. Thickness 300 nm

$$\frac{1}{E_r} = \frac{1 - \nu^2}{E} + \frac{1 - \nu_i^2}{E_i}, \quad (8.4)$$

where E and ν are the Young's modulus and the Poisson constant of the sample, respectively, and E_i and ν_i are the same parameters for the indenter.

According to Bulychev [10] and Shorshorov [11], motivated by Sneddon's method [12], this reduced Young's modulus can be related to the rigidity S measured at the maximum of the unloading curve by the relation

$$S = \frac{dP}{dh} = \beta \frac{2}{\sqrt{\Pi}} E_r \sqrt{A(h_c)}, \quad (8.5)$$

where β is a constant depending on the indenter geometry:

- $\beta = 1.034$ for a Berkovich indenter,
- $\beta = 1.012$ for a Vickers indenter,
- $\beta = 1.000$ for a spherical indenter.

A is the contact area (for a Vickers indenter) or the projected area of contact (for a Berkovich indenter) of the the elastic contact. The Young's modulus can be directly obtained by calculating the rigidity S :

$$E_r = \frac{\sqrt{\Pi}}{2\beta} \frac{S}{\sqrt{A(h_c)}}, \quad (8.6)$$

where S is the contact rigidity calculated in the first part of the unloading curve ($S = dP/dh$). Equation (8.6) is valid for any indenter with axial symmetry.

In nanoindentation several methods have been developed to determine the contact area. Pethica et al. [13] proposed a simple method based on the area

function of the indenter. Examining (8.6), the reduced Young's modulus can be calculated if the contact rigidity S and the contact area at the maximum of the curve can be determined independently. This means that the contact depth h_c must be known.

Determining the Contact Depth

The first approximation for h_c was proposed by Doerner and Nix [14], simply setting the contact depth equal to the plastic depth h_p . This approximation assumes that the unloading curve can be identified with its tangent at maximal load. However, it proved inadequate for acquiring a good hardness measurement. It is preferable to calculate the contact depth at the maximal depth and load for which the material fits perfectly against the shape of the indenter. In this case the contact depth h_c is expressed as a function of h_{\max} and h_s :

$$h_c = h_{\max} - h_s . \quad (8.7)$$

Since h_{\max} is easily measured, the problem here amounts to determining the elastic displacement h_s of the surface. For a conical indenter, Sneddon [12] showed that h_s can be written as a function of the final depth h_f :

$$h_s = \frac{\pi - 2}{\pi} (h_{\max} - h_f) . \quad (8.8)$$

This relation is valid only in the elastic part of the displacement. Sneddon [12] also showed that the quantity $h - h_f$ can be written in the form

$$h_{\max} - h_f = 2 \frac{P_{\max}}{S} . \quad (8.9)$$

Oliver and Pharr [8] then showed from (8.8) and (8.9) that h_s could be expressed as

$$h_s = \varepsilon \frac{P_{\max}}{S} , \quad (8.10)$$

where $\varepsilon = 0.72$ for a conical indenter.

This result can be generalised to other types of indenter in which only the value of ε changes. Empirically, $\varepsilon = 0.75$ for an indenter in the form of a paraboloid of revolution, and $\varepsilon = 1$ for an indenter with plane geometry.

For greater accuracy, a recent calculation presented by Pharr, Bolshakov et al. [15] has been used to refine the calculation of ε . This new expression can be used to find ε from experimental data via knowledge of the coefficient m . For this calculation, two hypotheses are required: it is assumed that the material is elastic and that the indenter is rigid.

From Sneddon's method [12], one can calculate the pressure P exerted on the sample:

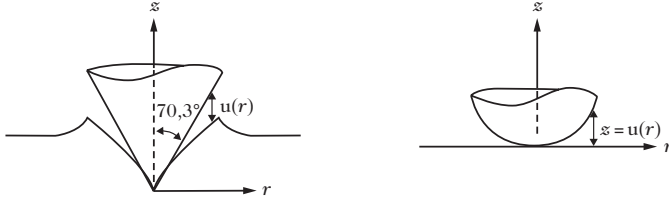


Fig. 8.13. Schematic representation of a non-ideal indenter

$$P = 2E_r \sqrt{\pi} B r^{n+1} \frac{n}{(n+1)} \frac{\Gamma\left(\frac{n}{2} + 1\right)}{\Gamma\left(\frac{n}{2} + \frac{1}{2}\right)}, \quad (8.11)$$

where $m = 1 + 1/n$, r is the radius of contact, B is a constant, E_r is Young's modulus, and Γ is the gamma function. The radius of curvature r is then given by

$$r = \left[\frac{\Gamma\left(\frac{n}{2} + \frac{1}{2}\right)}{B \sqrt{\pi} \Gamma\left(\frac{n}{2} + 1\right)} \right]^{1/n} (h - h_f)^{1/n}. \quad (8.12)$$

P can now be expressed in terms of the elastic response $h' = h - h_f$:

$$P = \frac{2E_{\text{eff}}}{(\sqrt{\pi}B)^{1/n}} \left(\frac{n}{n+1}\right) \left[\frac{\Gamma(n/2 + 1/2)}{\Gamma(n/2 + 1)} \right]^{1/n} h'^{1+1/n}. \quad (8.13)$$

This expression corresponds to the result obtained by Oliver and Pharr [8]:

$$\alpha = \frac{2E_{\text{eff}}}{(\sqrt{\pi}B)^{1/n}} \left(\frac{n}{n+1}\right) \left[\frac{\Gamma(n/2 + 1/2)}{\Gamma(n/2 + 1)} \right]^{1/n}. \quad (8.14)$$

To introduce the plasticity into their model, Oliver, Pharr and Bolshakov considered the deviation of the indenter from the ideal shape, as illustrated in Fig. 8.13. They approximated the shape of the indenter using a paraboloid correction described as illustrated in the figure:

$$Z = Br^n.$$

In this precise case, one may consider that $h_s = h_{\text{max}} - h_c = h_{\text{max}} - Br^n$.

Making the approximation that h_s tends to h_f and substituting what corresponds to the purely elastic part in the expression (8.13) for P , the following expression for ε is obtained from (8.10):

$$\varepsilon = m \left[1 - \frac{2\Gamma\left(\frac{m}{2(m-1)}\right)}{\sqrt{\pi}\Gamma\left(\frac{1}{2(m-1)}\right)} \right]. \quad (8.15)$$

As a last remark, note that h_s does not correspond exactly to the elastic part (which is equal to P_{\max}/S), but to a fraction ε of the latter.

Calculating the Hardness

The hardness H is defined by the average pressure sustained by the material under the indenter. It is expressed as the ratio of the applied load P to the contact area. In practice,

$$H = P_{\max}A(h_c), \quad (8.16)$$

where P_{\max} is the maximal load and $A(h_c)$ is the contact area at maximal load and depth.

Calibrating the Nanoindenter

Determining the Compliance of the Indenter. The compliance is defined as the reciprocal of the rigidity:

$$C = \frac{1}{S} = \frac{dh}{dP}. \quad (8.17)$$

The instrument influences the total compliance and interpretation of loading/unloading curves. Indeed, the measured displacement is the sum of the true displacement and a component due to the compliance of the instrument.

Modelling the instrument and sample by two springs in series shows that the total or measured compliance can be written

$$C = C_{\text{instr}} + C_{\text{sample}}, \quad (8.18)$$

where C_{sample} is the compliance of the sample calculated from (8.6):

$$C_{\text{sample}} = \frac{\sqrt{\pi}}{2\beta E_r} \frac{1}{\sqrt{A(h_c)}}. \quad (8.19)$$

The total compliance is then given by

$$C = C_{\text{instr}} + \frac{\sqrt{\pi}}{2\beta E_r} \frac{1}{\sqrt{A(h_c)}} = C_{\text{instr}} + \frac{\sqrt{\pi}}{2\beta E_r} \frac{\sqrt{H}}{\sqrt{P_{\max}}}, \quad (8.20)$$

where $S_{\text{instr}} = 1/C_{\text{instr}}$ is the rigidity of the instrument, $S = 1/C_{\text{sample}}$ is the contact rigidity, S_{spring} is the rigidity of the column spring, and C_{damp} is the damping coefficient.

If the Young's modulus is constant, C_{instr} can be obtained from a plot of $C = f(1/\sqrt{P_{\max}})$. The procedure then is to carry out several tests on a calibrating material (see Fig. 8.14).

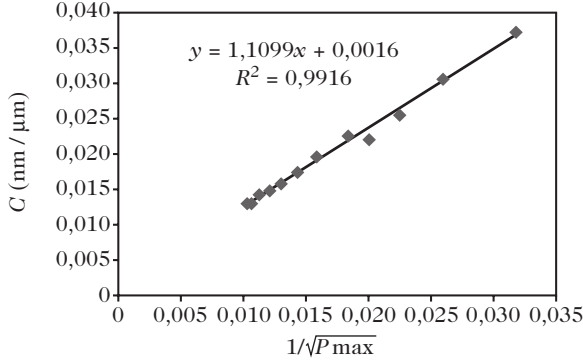


Fig. 8.14. Determining the compliance. Here $C_{\text{instr}} = 1.6 \text{ nm/mN}$

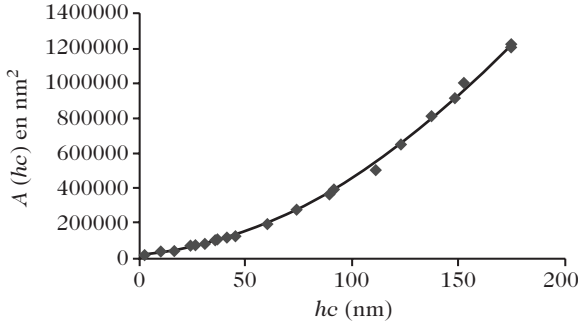


Fig. 8.15. Area function for a Berkovich indenter

Determining the Area Function $A = f(h)$. For an ideal indenter, the area A can be related to the plastic depth h_p by $A(h_c) = 24.5h_c^2$. The contact area is generally written in the form of a polynomial expansion:

$$A(h_c) = 24.5h_c^2 + C_1h_c^1 + C_2h_c^{1/2} + C_3h_c^{1/4} + \dots + C_8h_c^{1/128}, \quad (8.21)$$

where the coefficients C_1, C_2, \dots, C_8 are constants to be determined by a procedure described below. The procedure consists in making a large number of indents at different penetration depths on a calibration material (see Fig. 8.15). The contact area is calculated from (8.18) in each case.

Causes of Error and Precautions: The Pile-up Phenomenon

The so-called pile-up phenomenon [18] occurs in soft materials such as aluminium and leads to matter rising up around the indent, as shown in Fig. 8.16. This produces an error in the depth measurement, and in particular in the measurement of h_c . This kind of effect can lead to an underestimate of the contact area by a factor of as much as 40% and hence to an overestimate of the hardness and the Young's modulus.

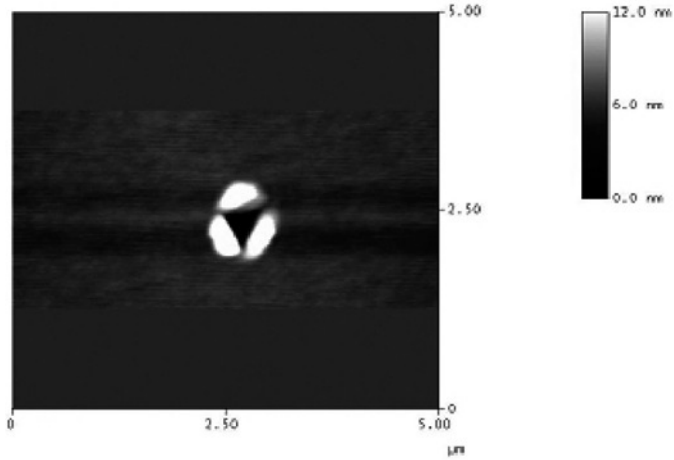


Fig. 8.16. Pile-up phenomenon as viewed by atomic force microscopy

A simple way of checking whether pile-up has occurred is to calculate the ratio h_f/h_{\max} , easily deduced from the loading/unloading curve. This ratio lies between 0 and 1. The minimal value corresponds to the perfectly elastic case and the maximal value to the case where no elastic recovery is observed. Using finite element analysis, Bolshakov et al. [19] showed that pile-up can be significant.

When there is a high level of pile-up, h_c can be calculated from a formula due to Loubet et al. [20, 21] which takes into account the ridges pushed up around the edge of the indent. These authors consider (by definition) that the plastic part satisfies

$$h_r = h - P/S. \quad (8.22)$$

Experimentally, they find that the plastic part h_r is proportional to the rigidity S . Applying the same approach as Sneddon [12], one then obtains

$$h_c \propto S \quad (\text{because } h_c \propto \sqrt{A}). \quad (8.23)$$

The main assumption in this calculation is that Young's modulus E should be constant throughout the thickness affected by the indentation.

Assuming that the indenter tip is not perfect, the rigidity can be rewritten as a function of h_i (see Fig. 8.17), which gives

$$S = B(h_r + h_i). \quad (8.24)$$

Finally, these authors define

$$h_c = \alpha(h_r + h_i), \quad (8.25)$$

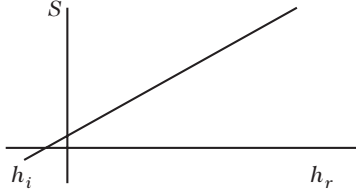


Fig. 8.17. Rigidity as a function of the plastic strain h_r

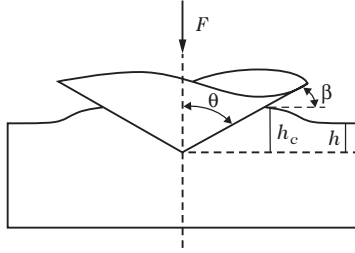


Fig. 8.18. Definition of β

where h_i corresponds to the tip imperfection and α is a constant with value $\alpha = 1.2$ for a Berkovich tip.

From this value of h_c , one can deduce the contact area

$$A = \beta[\alpha^2(h_r + h_i)^2] , \quad (8.26)$$

where β is called a shape factor. The Sneddon formula then gives the rigidity S and Young's modulus E_r as [12]

$$S^2 = \frac{4E_r^2 A}{\pi} , \quad (8.27)$$

$$E_r = \frac{B\sqrt{\pi}}{2\sqrt{\beta}\alpha} . \quad (8.28)$$

It should be noted that β comes from Sneddon's calculation and α and B from Loubet's. Bucaille et al. [21] used simulation to obtain the value $\alpha = 1.2$. In this case, using (8.25), h_c can be recalculated to give

$$h_c = \alpha(h_r + h_i) = \alpha(h - P/S) , \quad \text{where } \alpha = 1.2 ,$$

for a Berkovich tip, which corresponds to the situation described in Fig. 8.18.

It is important to note that, in this model, h_c is proportional to the plastic part and that, in contrast to Oliver and Pharr's model [8], the whole elastic part is taken into account to obtain the plastic part. Moreover, the ridge effect is such that h_c is greater than h_{\max} .

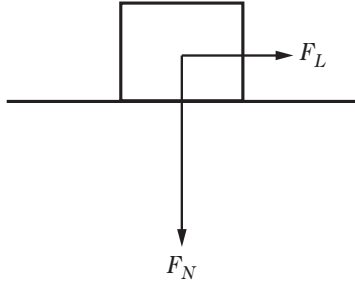


Fig. 8.19. Macroscopic forces relevant to contact between two solids

To conclude, in the presence of an elastoplastic material, one must use the model (8.14) due to Oliver and Pharr. In the presence of a soft material with a sizeable ridge around the edge of the indent, the expression for h_c given by the model due to Loubet and Bucaille [21] comes closer to the mark.

Mechanical Characterisation in Tribology. Nanoscratch Tests and Friction

Definition of Friction

The friction between two solid surfaces is defined by a coefficient. There corresponds a value to each regime, static or dynamic. We thus define:

- for the static regime, $\mu_s = F_{LS}/F_N$,
- for the dynamic regime, $\mu_d = F_{LD}/F_N$,

where F_{LS} and F_{LD} are the lateral forces required to initiate slipping and maintain the motion, respectively, and F_N is the applied normal force (see Fig. 8.19). For dry contact, $\mu_s < \mu_d$. In the present discussion, we shall be mainly concerned with the dynamic regime.

To characterise friction, the tools used to measure quantities such as forces or displacements depend mainly on the structure of the systems under consideration. Hence, for a homogeneous solid medium, a conventional triboscope is used, such as the pin-on-disk tribometer. For a nanostructured sample, one seeks information on the scale of the structure, i.e., the nanoscale. One can therefore define three length ranges appealing to very different apparatus (see Fig. 8.20).

Standard Model Due to Bowden and Tabor

Physical modelling of the phenomena underlying friction was first undertaken around 1950 by Bowden and Tabor [22]. This model takes into account the roughness of the surfaces in contact, which gives rise to shearing of adhesive microjunctions and ploughing by surface asperities. This is expressed by two contributions to the lateral force:

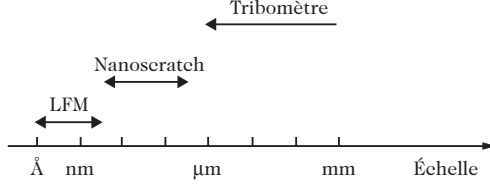


Fig. 8.20. Three length scales for tribological measurements

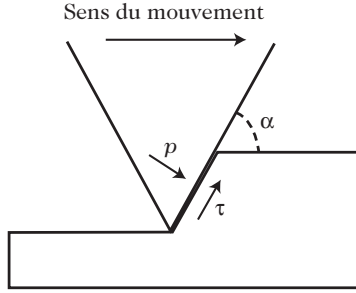


Fig. 8.21. Indenter in scratch mode

$$F_L = F_{LS} + F_{LP} = \tau A_{TC} + \mu_L F_N ,$$

where F_{LS} and F_{LP} are the lateral forces related to shear and ploughing, respectively, τ is the shear stress, and A_{TC} is the true area of contact. A_{TC} decreases as the roughness increases. The apparent contact area A_{AC} is always greater than A_{TC} .

When asperities have rather flattened profiles, the ploughing phenomenon can be neglected in comparison to shear. In this case, we have

$$\mu = \frac{F_L}{F_N} \approx \frac{\tau A_{TC}}{H A_{TC}} = \frac{\tau}{H} ,$$

where H and τ are then the plastic hardness and the shear stress of the least hard material.

Scratch Test

The plastic strain mode is conditioned by the shape of the indenter (see Fig. 8.21). Hence, depending on its apex angle, the predominant mechanism will be either shear or ploughing. Indeed, the friction coefficient can be expressed in terms of the shear and compression stresses, τ and p , respectively:

$$\mu = \frac{F_L}{F_N} = \frac{p \sin \alpha + \tau \cos \alpha}{p \cos \alpha - \tau \sin \alpha} .$$

So we have a context of pure shear when the angle α tends to zero, and ploughing when τ tends to zero.

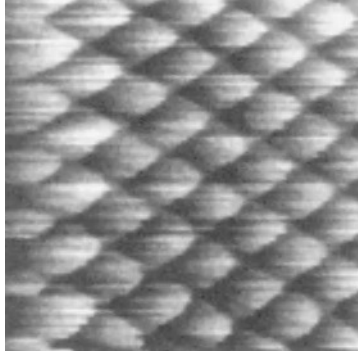


Fig. 8.22. Lateral force map obtained in LFM mode on a graphite surface. The scanned area is $2\text{ nm} \times 2\text{ nm}$. From [24], ©American Physical Society 1987

Lateral Force Microscope (LFM)

This mode of operation of the atomic force microscope (AFM) is used to probe outer surface tribological properties. It was developed at the end of the 1980s [23, 24]. In topographic imaging mode, a system of photodiodes is used to measure the change, in the vertical direction, of the path of the laser beam reflected by the cantilever arm holding the AFM tip. In LFM, in contact mode, a normal force is applied and the tip scans the surface, whilst measuring the change in path of the same laser beam but this time in the horizontal direction. This change of path is caused by torsion in the cantilever arm. Given the mechanical characteristics of the cantilever (stiffness constant, etc.), information can be deduced concerning the lateral force. Finally, as the tip scans the surface, a map of the lateral force can be produced on the atomic scale. This is illustrated for a graphite surface in Fig. 8.22.

Figure 8.23 shows the change in the lateral force as a function of the lateral position x on the same sample. The oscillation phenomenon known as stick-slip motion is clearly visible. As the name suggests, it corresponds to motion in a series of stops and starts, caused directly by the crystal structure of the material. The tip-surface interaction remains elastic and no wear is observed. The phenomenon of hysteresis observed between the outward and return journey of the tip is due to energy dissipation [21]. Indeed, the measured response signal contains a reversible elastic part and a dissipative part. The image obtained depends closely on the crystal structure of the surface under investigation. The measured lateral force can be described by a surface potential of the form

$$V_S = V_0 \cos(k_x x) e^{-k_z z} .$$

This gives $F_L = k_x V_0 \sin(k_x x) e^{-k_z z}$.

Although this experiment provides local information, it remains semi-quantitative. Indeed, it is a delicate matter to describe the mechanical be-

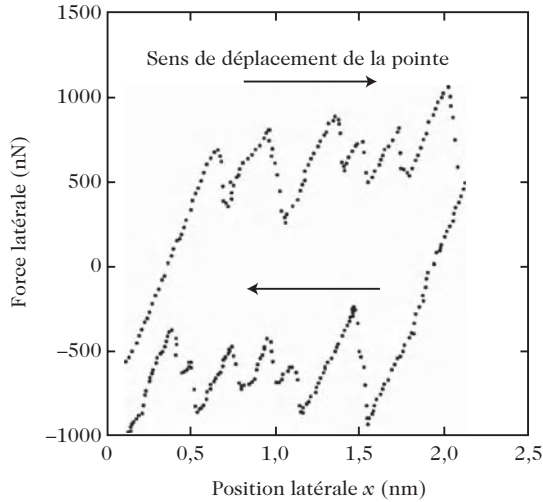


Fig. 8.23. Change in lateral force as a function of the lateral position of the tip [20]

haviour of the cantilever with any accuracy, and all the more so when it is under torsion. This is why other methods have been developed. These are systems in which the tip is no longer carried by a cantilever, such as the nanoscratch experiment, even though the spatial resolution is no longer as good as with LFM.

Nanoscratch Test

This type of measurement uses the same type of tip as nanoindentation. This may be an axially symmetric (e.g., conical, spherical) or pyramidal (Berkovich) tip. A first fundamental difference with respect to the LFM method is the characteristic size of the ‘active’ part of the tip. Whereas the tips used in LFM, made from silicon nitride, have a radius of curvature at the apex of nanometric order, which corresponds to a few atomic sites, the tips used in nanoscratch tests, generally made from diamond, have characteristic size around a hundred nanometers. A direct consequence is the loss of atomic lateral resolution. On the other hand, normal forces applied in the nanoscratch test can reach 1 mN. With such forces, these tests are able to investigate both plastic strain and wear. For a metallic film, the penetration depth can be as much as 100 nm.

The system developed by Hysitron is based on a double capacitive sensor, as shown in Fig. 8.24. Each sensor comprises three plates, one of which is mobile and connected to the tip. The first sensor is used to exert a normal load by applying a tension between the moving plate on which the tip is mounted and a fixed plate. The second capacitive sensor imposes the lateral displacement of the tip and measures the lateral resistance force. This provides quantitative information concerning normal and lateral forces and displacements.

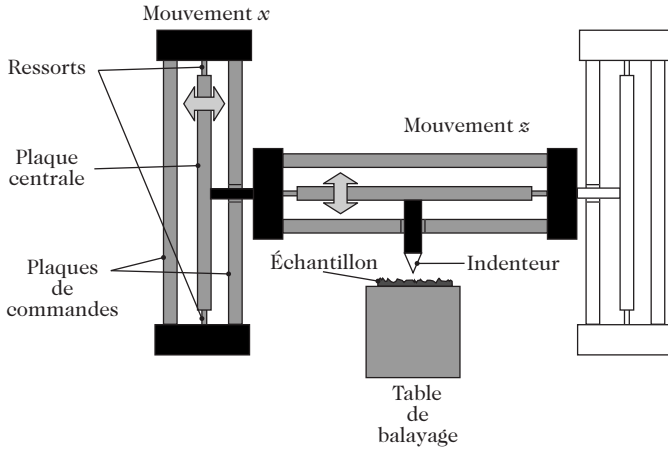


Fig. 8.24. Mode of operation of the double capacitive sensor

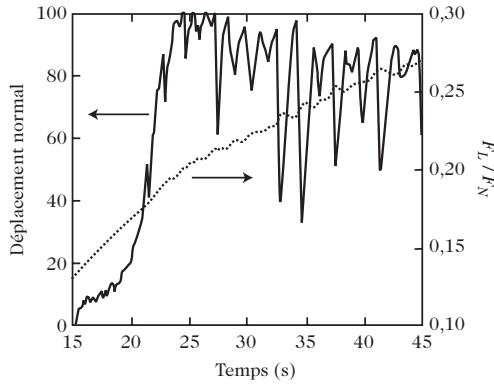


Fig. 8.25. Time dependence of the normal displacement (*left-hand scale*) and the ratio F_L/F_N (*right-hand scale*) during a nanoscratch test on a Ti/TiN multilayer

In the case of nanomaterials and in particular multilayers with nanometric periods, this system can provide local tribological information. Figure 8.25 shows the time variation of the ratio F_L/F_N and the normal displacement of the tip when the latter is subject to a lateral displacement at constant speed of the order of $0.5 \mu\text{m/s}$ and a normal load varying from 0 to $1500 \mu\text{N}$. The case illustrated is a multilayer made by PVD and comprising ten Ti/TiN layers. Each layer of Ti/TiN has thickness $5 \text{ nm} + 5 \text{ nm} = 10 \text{ nm}$. The observed oscillations can thus be directly related to the nanometric strata of the multilayer. It would have been impossible to observe this phenomenon using conventional tribology.

Using this method, one can also study plastic deformation mechanisms during the test. The importance of the way the normal load is applied can

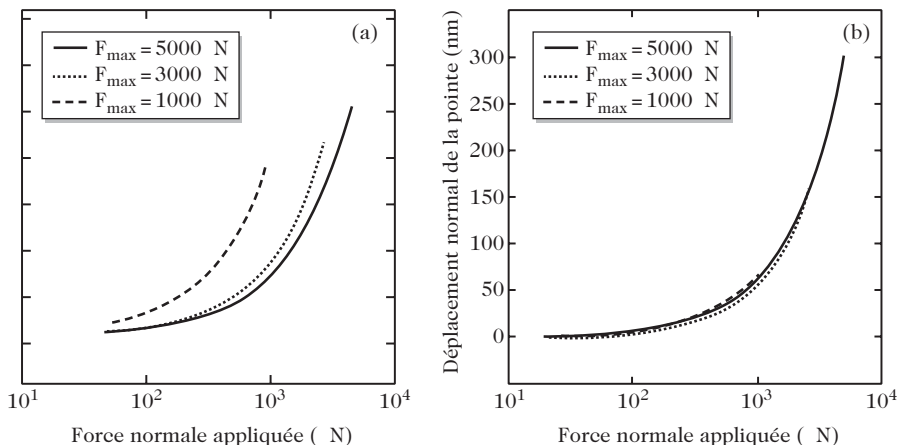


Fig. 8.26. (a) Variation of the normal displacement of the tip as a function of the normal force applied during the nanoscratch test: dx/dt constant and dF_N/dt variable. (b) Same quantities measured under the same deformation conditions but with dx/dt variable and dF_N/dt constant

thus be demonstrated. Figure 8.26 shows the normal displacement curves as a function of the applied normal load during nanoscratch tests over a time span that is held constant but with different maximal normal loads of 1 000, 3 000, 4 000 and 5 000 μ N. The sample here is a titanium nitride film of thickness 300 nm deposited by PVD on a silicon (100) substrate. The logarithmic scale of the normal force (horizontal axis) suggests the possibility of superposing all the curves by simple translation. On a linear scale, this amounts to applying a multiplicative factor. The calculation shows that this multiplicative factor amounts in turn to imposing a variation of the normal force that is constant in time, from one test to the next. This demonstrates the importance of the strain and wear regime during measurements.

8.2.2 Computer Modelling

Introduction

The development of nanomaterials used in nanotechnology as assembly structures demands an understanding of their mechanical properties on the nanoscale. Evaluating physical properties like the elastic modulus, the elastic limit under tension or compression, or the buckling stress constitutes a real challenge for nanomechanics research owing to their experimental inaccessibility. Moreover the experimental validity of such results can only be upheld if the measurements are fully repeatable, and this involves large numbers of samples and a consequent high cost in many cases. To help experimenters and theoreticians alike to improve understanding of these nanomaterials by means of computer

simulations, it is essential to develop well-suited models, i.e., models with reasonable numerical cost.

When analysing mechanical behaviour, there are two main approaches to modelling: either using direct methods based on molecular dynamics, or using ‘continuum’ methods developed to study the mechanics of solids or structures. These two approaches make different use of results obtained in molecular mechanics, which is an empirical method resulting from fitting simple mathematical functions to experimental results. Molecules are treated as assemblies of atoms subject to repulsive and attractive force fields resulting from interaction potentials between these atoms. This theoretical framework deviates in several ways from the one provided by quantum mechanics, but it is much less costly in calculation time and molecules comprising several thousand atoms can be modelled in this way.

Molecular dynamics provides a nanoscale description of the motions and spatial evolution of molecules. Each atom is treated as a point mass vibrating about its equilibrium position under the effects of thermal agitation and force fields defined by molecular mechanics. In practice, the idea is to solve Newton’s equations numerically using the Verlet algorithm [26]. Displacements are calculated explicitly, requiring very short time steps, of picosecond order, given the high frequencies contained in the model. Simulation periods are thus very short and the numerical cost soon becomes prohibitively high when large assemblies of molecules containing millions or even billions of atoms are considered to reproduce behaviour on microscopic or macroscopic scales. Recently, with the development of parallel computing, it has been possible to simulate behaviour on larger scales [27–29].

To characterise the mechanical behaviour, e.g., by identifying the elastic modulus or mechanical resistance, a quasistatic approach is preferable, in which vibrational dynamics is ignored. To reduce computation time still further, the interaction forces between atoms and their nearest neighbours can be modelled by beam-type assembly forces, so that the system becomes equivalent to a truss structure as conventionally studied in mechanics [30]. However, when studying large samples, the numerical cost is still rather large and a continuum approach is then required.

The continuum methods provide a macroscopic description of matter. Above a certain characteristic volume, the material has homogeneous behaviour defined by the laws relating strains to internal stresses on the macroscopic scale. These constitutive laws governing mechanical behaviour derive from a nonlinear hyperelastic potential which can be estimated from the interaction potentials between atoms. The solution is then obtained by the finite element method which discretises the continuum model into a set of elements of finite volume with dimensions greater than the characteristic volume. A finite element may correspond to several hundred or even thousand atoms depending on its dimensions, and this considerably cuts down the number of degrees of freedom of the system under investigation in comparison with a molecular dynamics model. In the case of crystals with sheet-like structure such as

graphene, it is possible to use finite surface elements. With these methods, one can no longer monitor the motions of individual atoms; it is rather the global behaviour of the whole structure that is under investigation. These studies may be either quasistatic or dynamic, and in the latter case only low frequency phenomena are accessible. Simulation times can be greater than in molecular dynamics, thereby reducing the numerical cost.

In the next section, we review the basic ideas of the finite element method, illustrating with examples of applications to the micro- and nanoscale. In these examples, one begins with a priori knowledge of the behaviour of the material on the macroscopic scale, without taking molecular mechanics into account. What is revealed here is the feasibility of the finite element method for investigating small scale multiphysical phenomena. In the second section, we discuss carbon nanotubes as a particularly well-developed field of industrial application in nanomechanics and in which the finite element method has been put to use by integrating the laws of molecular mechanics. In the third section, we give a brief discussion of work combining both molecular mechanics and finite elements in the context of multiscale approaches.

Application of the Finite Element Method

Engineering sciences such as solid and fluid mechanics or heat transfer provide ways of describing how physical systems behave by means of partial differential equations. The finite element method is one of the most widely used methods today for effective solution of such equations. It is a very general method that can be applied to most problems encountered in practice: stationary or non-stationary, linear or nonlinear, defined for arbitrary geometries. Furthermore, it can be easily adapted to heterogeneous media and multiphysical phenomena. Since Clough [31] first introduced the finite element method in 1960, many problems of mechanics and civil engineering have been solved using this approach. A great deal of work has been devoted to developing the theory. One should mention in particular the work of Marçal and King [32], who introduce the formulation of elastoplastic finite elements for small strains, Hibbitt et al. [33], McMeeking and Rice [34], who introduced the Lagrangian formulation for elastoplastic finite elements in the presence of large strains, and Zienkiewicz and Owen [35] who introduced the formulation of elasto-viscoplastic finite elements.

The constitutive equations most often used to model large strains in solids are the differential equations relating stress to strain rates. These laws must satisfy the principle of incrementally objective integration. Nagtegaal [36] and Hughes and Winget [37] proposed integration schemes for the constitutive equations in the presence of large deformations which respect incremental objectivity during finite time steps.

Among the various techniques used to integrate the constitutive equations, one in particular has steadily grown to become almost unanimously accepted: this is the radial return algorithm, developed by Wilkins in 1964 [38] for the

theory of small strains and then resurrected and generalised by Krieg and Krieg in 1977 [39]. Moreover, in this field, the idea of consistent linearisation introduced by Nagtegaal [36] and extended by Simo and Taylor [40] has been used to generate genuinely efficient tangential stiffness matrices for both small and large strain problems.

The finite element method is based on one simple idea: to discretise a complex geometrical shape by subdividing it into a large number of elementary subregions with simple geometrical shape (finite elements), interconnected at points called nodes. We consider the mechanical behaviour of each element separately, then piece these elements together in such a way that forces balance and displacements are compatible at each node.

In each element, simple approximations are used for the unknown variables to transform the partial differential equations into algebraic equations. The nodes and elements do not necessarily have any specific physical meaning but are based on considerations of accuracy in the approximation.

In a general context, the equation of motion of a deformable body can be expressed in the following matrix form:

$$M\ddot{\mathbf{u}} + C\dot{\mathbf{u}} + \mathbf{F}_{\text{int}} - \mathbf{F}(t) = 0 ,$$

where \mathbf{F}_{int} is the internal force vector and \mathbf{F} the external load vector, possibly a function of time t . M is the mass matrix, C the damping matrix, $\dot{\mathbf{u}}$ the velocity vector, and $\ddot{\mathbf{u}}$ the acceleration vector. In the particular case of linear static analysis in solid and structural mechanics, we have

$$K\mathbf{u} = \mathbf{F} ,$$

where K is the rigidity matrix of the system, \mathbf{u} the vector of unknown variables, i.e., displacements of the nodes, and \mathbf{F} the vector of known loads applied at the nodes.

The logical stages of the calculation by finite elements can be summarised as follows:

- Define nodes and elements (determine the mesh).
- For each element, establish the elementary matrices relating the nodal degrees of freedom to the forces applied at the nodes.
- Assemble elementary vectors and matrices into a global system in such a way as to satisfy equilibrium conditions at nodes.
- Modify the global system to account for boundary conditions.
- Solve the modified global system to obtain the displacements of the nodes.
- Calculate the gradients (strains and stresses) within the elements and the reactions at the nodes upon which boundary conditions are imposed.

From a practical point of view, calculation codes generally comprise three functional processors:

Preprocessor

- Choose the type of elements.
- Enter the geometrical properties.
- Enter the physical parameters.
- Create the geometric model.
- Create the mesh by defining nodes and elements.
- Apply loads.
- Impose boundary conditions.

Solver

- Choose the type of analysis (static, dynamic, etc.).
- Construct elementary vectors and matrices.
- Assemble elementary vectors and matrices to obtain a global system.
- Take into account boundary conditions.
- Solve the global system of equations.
- Calculate additional variations (stresses, reaction forces, etc.).

Post Processor

- Present the results in an intelligible and synthesised way in numerical or graphical form.
- Carry out complementary functions such as combination, animation, interpolation, or interpretation.

The finite element method has recently been applied to problems at small scales. We shall now present a few examples of these applications.

Plasma Projection

Plasma projection techniques have been successfully used in industry for many years to produce coatings that resist corrosion, oxidation, wear, and so on. The formation of a coating is a multiphysical problem, involving impacts of molten particles on the substrate, heat transfer between particles and substrate, and flattening out and solidification of the particles. The first example is a simulation of this multiphysical problem by the finite element method [41]. In order to provide an adequate treatment of the large strains occurring during impact, we have developed a remeshing technique. Figure 8.27 shows the temperature field of the liquid particle and the substrate at different times. The two curves show the time variation of the temperature at the centre of and outside the particle. Note that the rates of flattening and heat transfer are very high and that the particle is very small, having a diameter of only $50\ \mu\text{m}$.

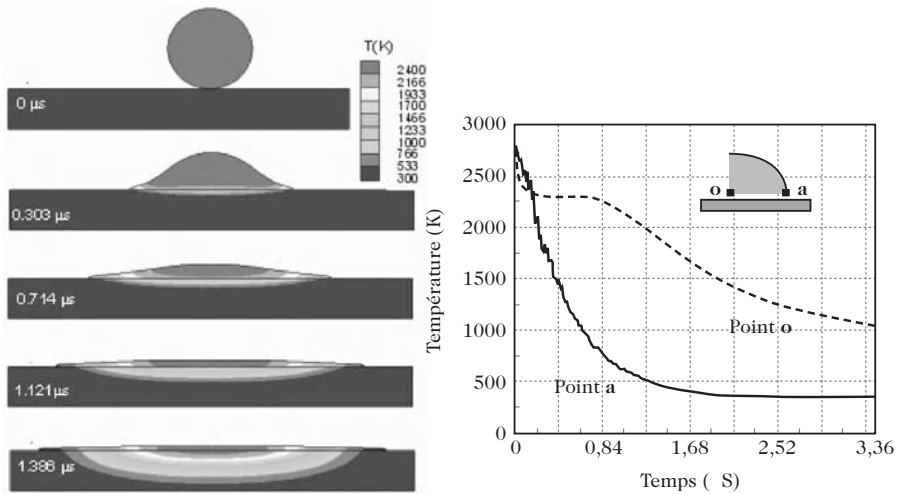


Fig. 8.27. Temperature field at different times during flattening. See also the colour plate

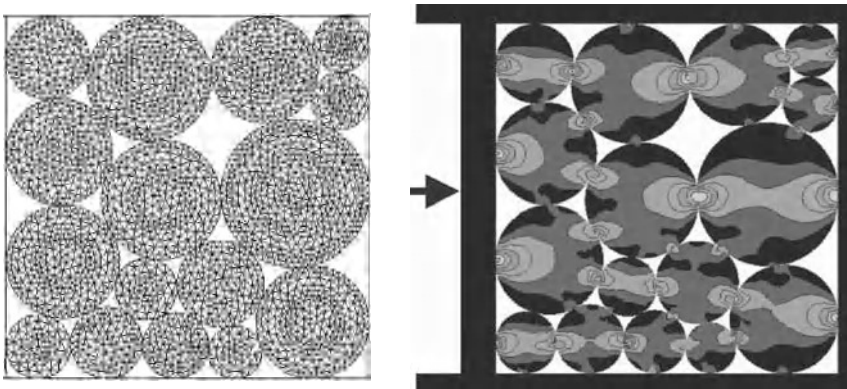


Fig. 8.28. Multiple contacts between particles. Mesh and constant value contours of the von Mises stresses

Representative Volume Element

The representative volume element (RVE) plays a key role in determining the effective properties of heterogeneous materials. Numerical computation is an essential tool for establishing the characteristic behaviour within this volume under external loading. The second example thus deals, for the first time, with this problem of multiple contacts between deformable particles, where the behaviour of each particle can be either elastic or hyperelastic. The finite element method is used to discretise the particles and obtain the stress field within each one, as shown in Fig. 8.28. In order to treat the problem of

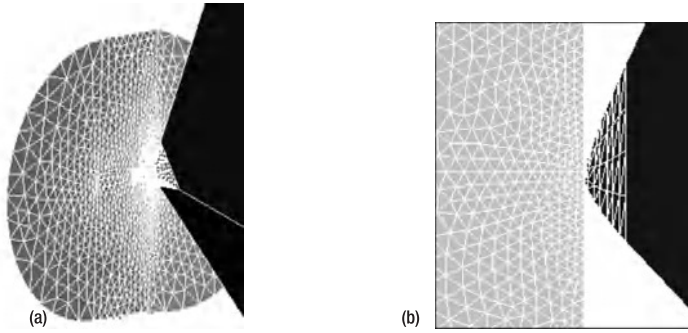


Fig. 8.29. Nanoindentation. Mesh

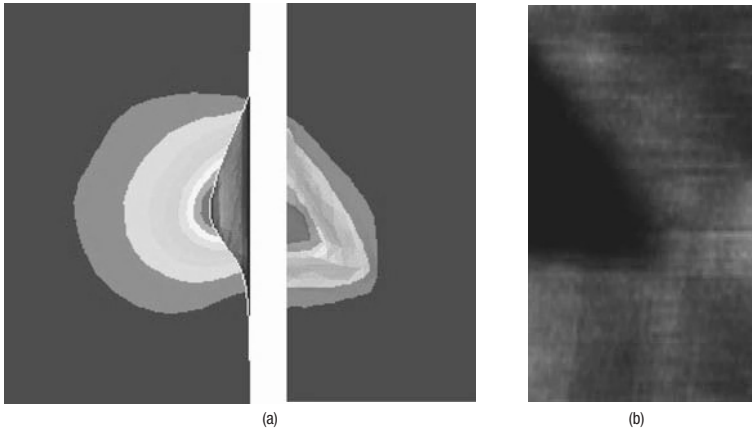


Fig. 8.30. Nanoindentation. (a) Numerical simulation. (b) Experimental result. See also the colour plate

frictional contact between the particles in an adequate way, a new approach was developed by Feng [42].

Nanoindentation

The third example is a model for nanoindentation. A tetrahedral (Berkovich) indenter comes into contact with the surface of a thin film (thickness 300 nm) on a substrate (different types of film being tested on different types of substrate). The thin film is assumed to have elastoplastic behaviour. The indenter is assumed to be rigid and to have a blunted tip with radius of curvature about 50 nm. Figure 8.29 shows the 3D meshed model and a more detailed 2D model. Note that the symmetry of the model is used to reduce computation time. Figure 8.30a shows the indent left on the surface and the stress distribution around the indentation region. The triangular shape of the indent faithfully reproduces what is observed experimentally on these scales (Fig. 8.30b).

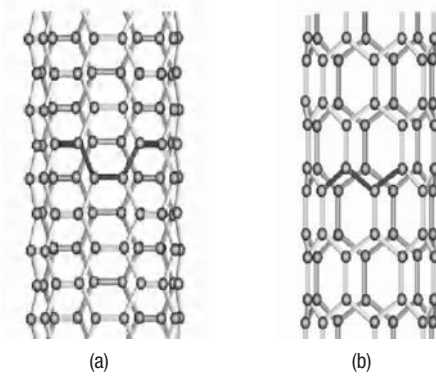


Fig. 8.31. Carbon nanotubes. (a) Armchair configuration. (b) Zigzag configuration

Simulation of Carbon Nanotubes

Carbon nanotubes are one of the main industrial products in the field of nanotechnology. They appear spontaneously when graphite is evaporated under the effect of an electrical discharge between two electrodes placed in a rare gas such as helium. These objects have molecular dimensions and are formed from one or more tiny carbon sheets arranged in concentric cylinders of diameter 1–10 nm (depending on the number of sheets) and length several microns, closed at the ends by spherical caps. The crystal structure of these carbon sheets, called graphenes, is hexagonal, while the crystal structure of the caps is pentagonal. Sumio Iijima, a Japanese scientist, was the first to observe them under the electron microscope in 1991 [43]. The way the graphene rolls up defines a parameter called the helicity which characterises the different types of nanotube. The helicity is specified by the chiral angle θ between the axis of the cylinder and the direction of one side of the hexagon. The configurations known as zigzag and armchair nanotubes are characterised by the values $\theta = 0$ and 30° , respectively (see Fig. 8.31). Given the hexagonal symmetry of the crystal lattice, θ lies between 0 and 30° .

Carbon nanotubes have remarkable physical properties with a wide range of potential applications in industry. For example, their elastic modulus is of the order of 1–5 TPa, well above the values for conventional carbon fibres, whilst remaining more flexible too [44]. The electrical properties of carbon nanotubes vary enormously with the diameter and helicity parameter, ranging from a semiconducting state to a metallic state. The helicity parameter also influences the mechanical properties [45].

Several theoretical models have been developed in the literature using the molecular dynamics approach [46, 47]. However, computation times can be prohibitive with these models, e.g., when simulating the behaviour of a bundle of multiwalled tubes involving a very large number of atoms. Another discrete approach has been put forward, treating the carbon nanotube as an

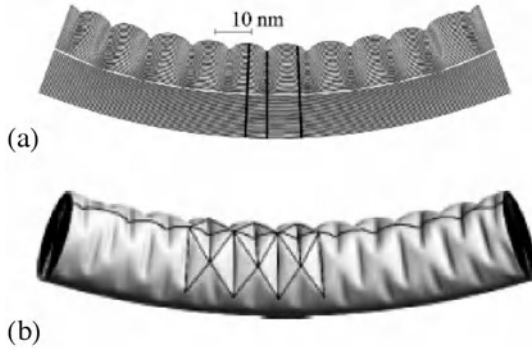


Fig. 8.32. Undulations of a 34-walled carbon nanotube. (a) Experimental observation in the plane of the tube axis [49]. (b) 3D simulation of the same [48]

assembled beam structure known as a truss in mechanics [30], in which the beam elements represent covalent binding forces between atoms. This type of model provides a static study and reduces calculations compared with the strictly molecular approach by restricting the atomic interaction of each atom to its nearest neighbours.

A continuum approach to modelling carbon nanotubes by the finite element method has been achieved by Arroyo and Belytschko [48]. It is based on a membrane model of strains in the carbon nanotube. Strains are calculated using the exponential Cauchy–Born rule to account for the effects of curvature of the tube. On the macroscopic level, stresses derive from a potential energy resulting from the sum over each finite element of the interaction energies between atoms bound according to the Tersoff–Brenner model of molecular mechanics. The interaction energy between atoms that are not bound together is also taken into account to model van der Waals forces according to the classical Lennard-Jones potential model, also from the field of molecular mechanics. These van der Waals forces operate between the carbon sheets in the case of multiwalled carbon nanotubes and between nanotubes when they form bundles.

Arroyo and Belytschko [48] present the results of a simulation of a carbon nanotube of length 124 nm, comprising 34 concentric carbon sheets, which corresponds to around 6 million atoms. The finite element model contains just 100 000 nodes, considerably reducing the size of the problem to be solved in comparison with a molecular dynamics simulation (by a factor of 60). The simulation reproduces the undulations observed experimentally in images obtained by transmission electron microscope (TEM) and published in [49] when the carbon nanotube is subject to flexion (see Fig. 8.32).

Figure 8.33 shows simulation results for a carbon nanotube under torsion, using molecular dynamics and finite elements. Good agreement is obtained between the two approaches.

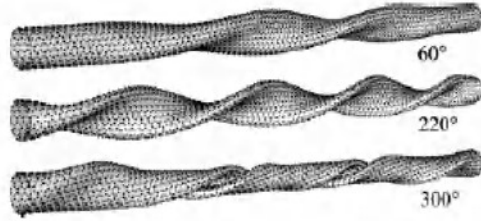


Fig. 8.33. Simulation of a carbon nanotube under torsion: molecular dynamics (*black dots*) and finite element (*grey surface*). Taken from [48] with kind permission of John Wiley & Sons

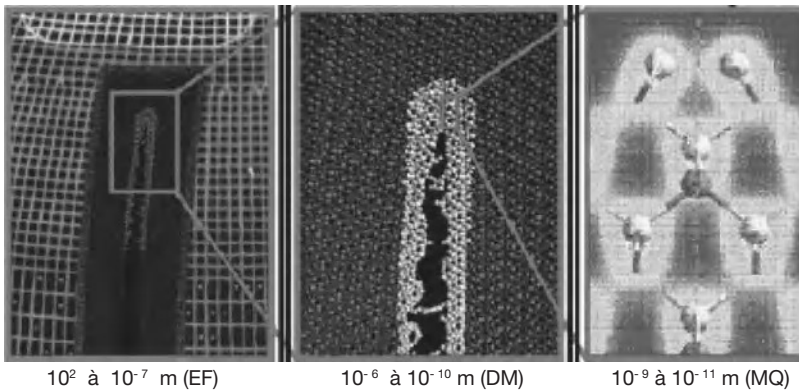


Fig. 8.34. Multiscale simulation. From [51], with the kind permission of Elsevier. See also the colour plate

Multiscale Simulations

The so-called multiscale simulation techniques were developed to obtain local quantum and molecular descriptions while retaining the continuum description on the global level, as illustrated in Fig. 8.34.

Several studies [50,51] have proposed ways of combining quantum mechanics (QM), molecular dynamics (MD), and finite elements (FE). In regions where the atoms obey the laws of continuum mechanics, the finite element method is used due to the advantages in terms of calculation time. However, in critical areas such as the extremity of a fracture, molecular dynamics and even quantum mechanics [e.g., *ab initio*, or density functional theory (DFT)] are required to obtain a more detailed study of the fracture process. The transition from the global to local levels involves a change of scale. More recently, Xiao and Belytschko [52] have proposed a way of improving the numerical compatibility between regions modelled by molecular dynamics and those modelled using the finite element method. At the interface between these two types of region, significant reflection effects are observed in the stress and

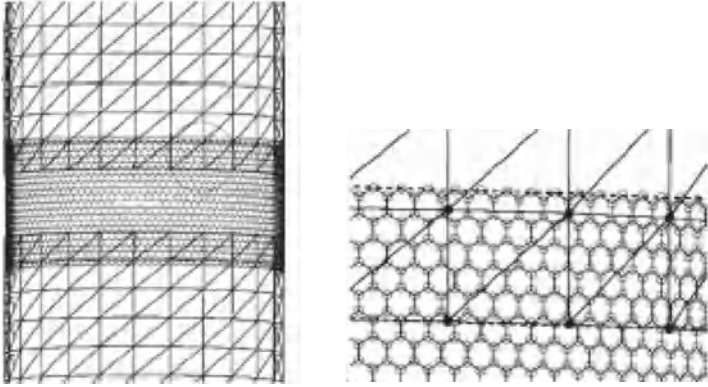


Fig. 8.35. Combined finite element and molecular dynamics (FE/MD). From [52], with the kind permission of Elsevier

strain fields, leading to unphysical distortion of the solution. The method suggested consists in introducing a rather broad transition region by superposing the finite element mesh of the continuum region on the atomistic structure of the molecular dynamics region, as can be seen in Fig. 8.35. In this region, the high frequencies generated by molecular dynamics are absorbed by the low frequencies of the continuum region.

Conclusion

Simulation is an important, even essential tool for aiding scientists to obtain a better understanding of the physical phenomena operating within nanomaterials. The examples discussed above, i.e., plasma projection, nanoindentation, and carbon nanotubes, show how one can get access to multiphysical phenomena at very short length scales (micron or nanometer) that are so difficult to observe experimentally. We have seen that, at these scales, a continuum approach by the finite element method can give excellent results, provided that certain precautions are taken. A good level of a priori knowledge concerning the constitutive laws and also a carefully chosen mesh are essential here. Understanding of the constitutive laws can be acquired a posteriori using molecular mechanics and/or quantum mechanics. The advantage with the finite element method as compared with molecular dynamics is that one can considerably reduce the number of degrees of freedom of the system under investigation, thereby reducing the numerical cost. The disadvantage is that one obtains a global description of the behaviour, thus losing any phenomenological description on the interatomic level, e.g., in problems of fracturing where propagation mechanisms must be determined). This is why the multi-scale approach seems to be a promising solution for simulating the behaviour of nanomaterials, combining as it does the finite element and molecular dynamics methods.

References

Macroscopic Mechanical Properties

1. T.D. Shen, C.C Koch, T.Y. Tsui, G.M. Pharr: On the elastic moduli of nanocrystalline Fe, Cu, Ni and Cu–Ni alloys prepared by mechanical milling/alloying, *J. Mater. Res.* **10**, No. 6, 2892 (1995)
2. M. Verdier, M. Fivel, B. Gilles: Some investigations on the effect of length scale on mechanical properties, *Adv. Eng. Mat.* **3**, No. 8, 597–601 (2001)
3. R.D. Mindlin: Second gradient of strain and surface tension in linear elasticity, *Int. J. Sol. Struct.* **1**, 417–418 (1965)
4. E. Cosserat, F. Cosserat: *Théorie des corps déformables*, A. Herman et Fils, Paris (1909)
5. J. Besson, G. Cailletaud, J.-L. Chaboche, S. Forest: *Mécanique non-linéaire des matériaux*, Hermes Science Publication, Paris (2001)
6. A.C. Eringer: *Polar and Non-Local Field Theories*, Continuum Physics, ed. by A.C. Eringer, Vol. IV, Academic Press (1976)

Nanomechanical Properties: Experimentation

7. B. Bhushan: *Micro/Nanotribology*, CRC Press, Florida, USA (1995)
8. W.C. Oliver, G.M. Pharr: *J. Mater. Res.* **7**, 1564 (1992)
9. D. Tabor: *The Hardness of Solids*, Oxford, Clarendon Press (1951)
10. S.I. Bulychyev, V.P. Alekhin, M.Kh. Shorshorov, A.P. Ternovskii, G.D. Shnyrev: *Zavod. Lab.* 1137 (1975)
11. M.Kh. Shorshorov, S.I. Bulychyev, V.P. Alekhin: *Sov. Phys. Dokl.* **26**, 769 (1982)
12. I.N. Sneddon: *Int. J. Eng. Sci.* **3**, 47 (1965)
13. J.B. Pethica, R. Hutchings, W.C. Oliver: *Philos. Mag. A* **48**, 593–606 (1983)
14. M.F. Doerner, W.D. Nix: *J. Mater. Res.* **1**, 845–851 (1986)
15. G.M. Pharr, A. Bolshakov: *J. Mater. Res.* **17**, No. 10, 2660–2669 (2002)
16. H. Hehtz, J. Reine: *Angewandte Mathematik*, **92**, 156 (1882)
17. J. Boussinesq: *Applications des potentiels à l'étude de l'équilibre et du mouvement des solides élastiques*, Gauthier-Villars, Paris (1885)
18. B. Bushan, S. Sundararajan: *Acta Mater.* **46**, 3793 (1998)
19. A. Bolshakov, W.C. Oliver, G.M. Pharr: *Pittsburgh, Materials Research Society*, 141–146 (1997)
20. G. Hochstetter, A. Jimenez, J.L. Loubet: *J. Macromol. Sci. Phys. B* **38** (5 and 6), 681–692 (2004)
21. J.L. Bucaille, S. Stauss, E. Felder, J. Michler: *Acta Materialia* **51**, 1663–1678 (2003)
22. F.P. Bowden, D. Tabor: *The Friction and Lubrication of Solids*, Clarendon Press, Oxford (1950–1954)
23. J.-M. Georges: *Frottement, usure et lubrification*, Sciences et techniques de l'ingénieur, CNRS Editions, Eyrolles (2000)
24. C.M. Mate, G.M. McClelland, R. Erlandsson, S. Chiang: *Phys. Rev. Lett.* **59**, 1942–1945 (1987)
25. O. Pietrement: *Doctoral thesis, University of Reims* (2000)

Nanomechanical Properties: Computer Modelling

26. L. Verlet: Computer ‘experiments’ on classical fluids. I. Thermodynamical properties of Lennard-Jones molecules, *Phys. Rev.* **159**, 98–103 (1967)
27. P. Vashishta, R.K. Kalia, A. Nakano: Multimillion atom molecular dynamics simulations of nanoparticles on parallel computers, *J. Nanoparticle Research* **5**, 119–135 (2003)
28. M.J. Buehler, A. Hartmaier, H. Gao, M. Duchaineau, F.F. Abraham: Atomic plasticity: Description and analysis of a one-billion atom simulation of ductile materials failure, *Comput. Methods Appl. Mech. Engrg.* **193**, 5257–5282 (2004)
29. H. Auradou, M. Zei, E. Bouchaud: Numerical study of the temperature and porosity effects on the fracture propagation in a 2D network of elastic bonds, *Eur. Phys. J. B* **44**, 365–372 (2005)
30. C. Li, T.W. Chou: A structural mechanics approach for the analysis of carbon nanotubes, *Int. J. Solids Struc.* **40**, 2487–2499 (2003)
31. R.W. Clough: The finite element in-plane stress analysis, *Proc. ASCE Conf. on Electronic Computation* (1960)
32. P.V. Marçal, I.P. King: Elastic plastic analysis of two dimensional stress systems by the finite element method, *Num. Meth. Ind. Form. Swansea* **9** (1967)
33. H.D. Hibbitt, P.V. Marçal, J.R. Rice: A finite element formulation for problems of large strain and large displacement, *Int. J. Solids Struc.* **6**, 1069–1086 (1970)
34. R.M. McMeeking, J.R. Rice: Finite element formulation for problems of large elastic–plastic deformation, *Int. J. Solids Struc.* **11**, 601–616 (1975)
35. O.C. Zienkiewicz, D.R.J. Owen: Analysis of viscoplastic effects in pressure vessels by the finite element method, *Nuclear Engr. Des.* **28** (1974)
36. J.C. Nagtegaal: On the implementation of inelastic constitutive equations with special reference to large deformation problems, *Comp. Methods Appl. Mech. Eng.* **33**, 469–484 (1982)
37. T.J.L. Hughes, J. Winget: Finite rotation effects in numerical integration of rate constitutive equations arising in large deformation analysis, *Int. J. Num. Meth. Eng.* **15**, 1862–1867 (1980)
38. M.L. Wilkins: Calculation of elastoplastic flaws. In: *Methods in Computational Physics*, ed. by B. Alder, Academic Press (1964)
39. R.D. Krieg, B.D. Krieg: Accuracies of numerical solution method for the elastic–perfectly plastic model, *ASME, J. Pressure Vessels and Piping Div.* **99**, 510–515 (1977)
40. J.C. Simo, R.L. Taylor: Consistent tangent operator for rate-independent elasto-plasticity, *Comp. Methods Appl. Mech. Eng.* **48**, 101–118 (1985)
41. Z.Q. Feng: Sur la modélisation d’un problème multiphysique: la projection à plasma, 7th Colloque National en Calcul des Structures, Giens, France (17–20 May 2005)
42. Z.Q. Feng: 2D or 3D frictional contact algorithms and applications in a large deformation context, *Comm. Num. Meth. Eng.* **11**, 409–416 (1995)
43. S. Iijima: Helical microtubules of graphitic carbon, *Nature* **354**, 56–58 (1991)
44. M.M.J. Treacy, T.W. Ebbesen, T.M. Gibson: Exceptionally high Young’s modulus observed for individual carbon nanotubes, *Nature* **381**, 680–687 (1996)
45. V.N. Popov, V.E. Van Doren, M. Balkanski: Elastic properties of single-walled carbon nanotubes, *Phys. Rev. B* **61**, 3078–3084 (2000)

46. B.I. Yakobson, M.P. Campbell, C.J. Brabec, J. Bernholc: High strain rate fracture and C-chain unraveling in carbon nanotubes, *Computational Materials Science*, **8**, 341–348 (1997)
47. E. Hernandez, C. Goze, P. Bernier, A. Rubio: Elastic properties of C and BxCyNz composite nanotubes, *Phys. Rev. Lett.* **80**, 4502–4505 (1998)
48. M. Arroyo, T. Belytschko: Finite element methods for the non-linear mechanics of crystalline sheets and nanotubes, *Int. J. Numer. Meth. Engng.* **59**, 419–456 (2004)
49. T. Kuzumaki, T. Hayashi, H. Ichinose, K. Miyazawa, K. Ito, Y. Ishida: In-situ observed deformation of carbon nanotubes, *Phil. Mag. A* **77** (6), 1461–1469 (1998)
50. F.F. Abraham, J.Q. Broughton, N. Bernstein, E. Kaxiras: Spanning the length scales in dynamic simulation, *Comput. Phys.* **12** (6), 538–546 (1998)
51. S. Ogata, E. Lidorikis, F. Shimojo, A. Nakano, P. Vashishta, R.K. Kalia: Hybrid finite-element/molecular-dynamics/electronic-density-functional approach to materials simulations on parallel computers, *Comp. Phys. Comm.* **138**, 143–154 (2001)
52. S.P. Xiao, T. Belytschko: A bridging domain method for coupling continua with molecular dynamics, *Comput. Methods Appl. Mech. Engrg.* **193**, 1645–1669 (2004)